NANO · MICRO small
www.small-journal.com

Power Generation from Moisture Fluctuations Using Polyvinyl Alcohol-Wrapped Dopamine/Polyvinylidene Difluoride Nanofibers

*Tong Li, Fei Jin, Minghe Qu, Fan Yang, Jin Zhang, Tao Yuan, Wei Dong, Jie Zheng, Ting Wang, and Zhang-Qi Feng**

Despite the boom in the water-triggered electric power generation technologies, few attempts have been made with a broader horizon—yielding the electricity from sweat, which is of great value for low-power-consumption wearable electronics. Here, an electromechanical coupling and humidity-actuated two-in-one humidity actuator-driven piezoelectric generator (HAPG) are reported, that can yield continuous electric power from fluctuations in the ambient humidity. It is composed of polyvinyl alcohol (PVA)-wrapped highly aligned dopamine (DA)/polyvinylidene fluoride (PVDF) shell/core nanofibers (PVA@DA/PVDF NFs). As-received PVA@DA/PVDF NFs can exchange water with the ambient humidity to perform expansion and contraction and convert them into electric power. An all-fiber-based portable HAPG is fabricated and tested on human palm skin. The devices show high sensitivity and accuracy for converting the mental sweating-derived continuous moisture fluctuations into electric power. This electric power can be stored in capacitors, which is expected to power micro- and nano-electronic devices or be used in electrotherapy such as electrical stimulation to promote wound healing. Beyond this, the obtained voltage profiles exhibit unique features that can reflect the typical sweat damping oscillation curve features.

1. Introduction

With the rapid development of economics and the fast-growing demand for energy, clean and renewable energy has been of much significance and urgency.[1] Water, covering over 70% of the Earth's surface, contains tremendous energies including water wave energy, tidal energy, and ultrasonic energy which deserve to be developed.[2,3] This motivates various water-triggered electric power generation technologies to harvest these water energy sources owing to the abundance of water, the simple device setup, and the green chemistry involved,[3,4] which have been demonstrated as a promising strategy for clean energy harvesting. Nevertheless, subtle fluctuations in the ambient humidity especially caused by sweat evaporation are often overlooked. They are of great value for the realization of sustainable, low-power-consumption wearable electronics.

Recently, it is reported that the humidity actuator can continuously extract chemical potential energy out of fluctuations in the ambient humidity to perform mechanical work (i.e., expansion and contraction), resulting in rapid and continuous locomotion.[5–7] Electromechanical coupled generators are well known that they can automatically convert mechanical energy into electric power.[8,9] Among them, piezoelectric generator is extremely sensitive to weak mechanical deformations, which is expected to yield electrical power from the mechanical deformation of the humidity actuator. Therefore, in addition to the established framework, the humidity actuator-driven piezoelectric generator (HAPG) offers an alternative for harvesting electrical energy from ambient moisture. However, the actuating unit and the piezoelectric unit in the existing HAPG are mostly independent,[5,10] which usually results in a large amount of energy loss or the feedback signal to lag the external stimulus. To address this issue, here we developed an electromechanical coupling and humidity-actuated two-in-one

T. Li, F. Jin, M. Qu, J. Zhang, Prof. W. Dong, Prof. Z.-Q. Feng
School of Chemistry and Chemical Engineering
Nanjing University of Science and Technology
Nanjing 210094, P. R. China
E-mail: fengzhangqi1981@njust.edu.cn
Dr. F. Yang
Institute of Rail Transit
Tongji University
Shanghai 201804, P. R. China
The ORCID identification number(s) for the author(s) of this article can be found under https://doi.org/10.1002/smll.202102550.
T. Yuan
Department of Orthopedic
Nanjing Jinling Hospital
Nanjing 210002, P. R. China
Prof. J. Zheng
Department of Chemical and Biomolecular Engineering
The University of Akron
Akron, Ohio 44325, USA
Prof. T. Wang
State Key Laboratory of Bioelectronics
Southeast University
Nanjing 210096, P. R. China

DOI: 10.1002/smll.202102550

HAPG composed of polyvinyl alcohol (PVA)-wrapped highly aligned dopamine (DA)/polyvinylidene fluoride (PVDF) shell/core nanofibers (PVA@DA/PVDF NFs), which showed high sensitivity and selectivity to humidity fluctuations with excellent stability. As we previously reported, DA/PVDF NFs were fabricated by one-step electrospinning on a large scale, which showed high piezoelectric property with excellent stability.[9] Therefore, high subtle humidity sensitivity was guaranteed due to it could respond well to the weak actuation deformation. Next, the -OH groups on DA shell of DA/PVDF NFs were responsible for the interface adsorption of PVA, stabilizing this PVA-DA-PVDF system. As a result, the two-in-one PVA@DA/PVDF NFs could act as the only component of HAPG. An all-fiber-based and preferred HAPG was fabricated and tested on human palm skin. The devices showed high sensitivity and accuracy for detecting subtle fluctuations in the ambient humidity-induced by various mental sweating. The obtained electric profiles exhibited unique features that could reflect the typical sweat damping oscillation curve features. The electrical energy could be stored in capacitors, which were expected to power wearable micro- and nano-electronic devices.

2. Results and Discussion

Our electromechanical coupling element was based on our recent work showing that the self-assembled DA shell on PVDF NF during the electrospinning process enhanced its piezoelectric performance and stability.[9] Inspired by the capability of cellulose microfibrils in plants to elicit directionality by anisotropically restricting the deformation of amorphous biogenic matrices,[7,11] the electromechanical coupled generator was highly aligned DA/PVDF NFs as the effective element. These aligned DA/PVDF NFs were fabricated by one-step electrospinning on a large scale, using U-shaped tube as the receiving device (**Figure 1**a,b, Figure S1, Supporting Information). The extensional forces provided by the good fiber alignment have been proven to further improve the energy generation efficiencies.[12] To test the piezoelectric performance of the aligned DA/PVDF NFs, a 30-µm-thick thin film was made by well-aligned DA/PVDF NFs with a size of 20 × 10 mm^2, and then integrated with top/bottom electrodes (Figure S2a, Supporting Information). The films were tested by repeatedly pressing and releasing at a pressure of ≈1 kPa and a low frequency of ≈1.2 Hz using an auto step-motor controller. The aligned arrays-based device yielded the output voltage of ≈18 V, which was higher than that (≈16 V) yield by the randomly stacking DA/PVDF NFs (Figure S2b, Supporting Information). Such high piezoelectric performance ensured a good response to the weak actuation deformation.

Considering the uniform distribution of −OH groups along its molecular chains and their potential strong interaction with the DA molecules on DA/PVDF NFs, PVA could form a shell layer with a thickness of ≈50 nm to wrap DA/PVDF NFs by simple suction filtration (the right of Figure 1c, Figure S3, Supporting Information). Molecular dynamic (MD) simulations further confirmed this molecular interaction (Figure 1d). Comparing the radial distribution functions (RDFs) of O atoms on PVA next to the $-NH_2$ groups (PVA−O—HN−DA) and next to the −OH groups (PVA-O—HO-DA), PVA−O—HO−DA RDF showed an obviously higher value in the range of <3 Å, confirming the PVA would preferably bond to the −OH groups on DA. While in DA/PVDF NFs, the -CF_2 groups on PVDF tended to bond with the $-NH_2$ groups on DA for aligning the PVDF chains and promoting β-phase nucleation as evidenced by our previous report (Figure S4, Supporting Information).[9] Therefore, the DA layer was a perfect bridge to build PVA-wrapped DA/PVDF NFs. Besides, many new mesoscopic joints were formed between PVA@DA/PVDF NFs (the left, Figure 1c), which significantly enhanced mechanical robustness and its internal stability (Figure S5, Supporting Information). Here, we chose PVA as the key component of the humidity actuator, mainly because PVA could spontaneously form hydrogen bonds with water molecules under ambient humidity and fix the water molecules to perform mechanical deformation (Figure 1e). To characterize the formation of hydrogen bonds, the IR of the PVA films from 10 to 85% relative humidity (RH) was obtained (Figure 1f). In the infrared spectrum, the shock absorption peaks of -OH were obtained from 3300 to 3500 cm^{-1}. As the humidity increased, the absorption peak of -OH moved toward the low wave (redshift). The redshift of the hydroxyl absorption peak occurred, because the hydrogen bond formed between the hydroxyl group of the PVA molecule and the water molecule reduced the overall electron cloud density, resulting in equal energy values.[13] Moreover, the higher the humidity, the larger the wavenumber of the redshift, indicating the formation of more hydrogen bonds that adsorbed more water molecules. MD simulation was used to further study the diffusion trajectory of water molecules in PVA. The entire calculation and simulation process reached equilibrium within 1000 ps, and we captured the initial and post-equilibrium pictures respectively as shown in Figure 1g. It could be intuitively seen from the captured equilibrium picture that, many water molecules diffused into the PVA region and resulted in its significant expansion. Such electromechanical coupling and humidity-actuated two-in-one PVA@DA/PVDF NFs showed excellent stability and avoided the potential delamination risk compared with other bilayer actuators.[10,14]

PVA@DA/PVDF film was programmable according to the direction of DA/PVDF NFs (**Figure 2**a). By anisotropically restricting the contraction stress along certain directions (e.g., $F_\perp$ of the longitudinal direction and $F_\parallel$ of the transverse direction) they also effectively directed the mechanical reconfiguration, thereby determining the mechanical effect. This could effectively reduce the dissipation of actuation mechanical energy.[15] These mechanical deformations could be automatically converted into electric power via PVA@DA/PVDF NFs (Figure S6, Supporting Information). Finite element analysis simulation confirmed that PVA@DA/PVDF NFs could convert mechanical deformation caused by the uniform stress load of the PVA into electrical power as reflected in the voltage contour (Figure 2b), in which PVA and DA/PVDF was modeled with the structural element solid185 and the piezoelectric element solid226, respectively. To quantify the ability of PVA@DA/PVDF NFs to extract water gradients, a 48-µm-thick thin film was made by highly aligned PVA@DA/PVDF NFs with a size of 5 mm × 30 mm. One end of the film was fixed on the base of the tensile tester, and the other end was flexible and movable

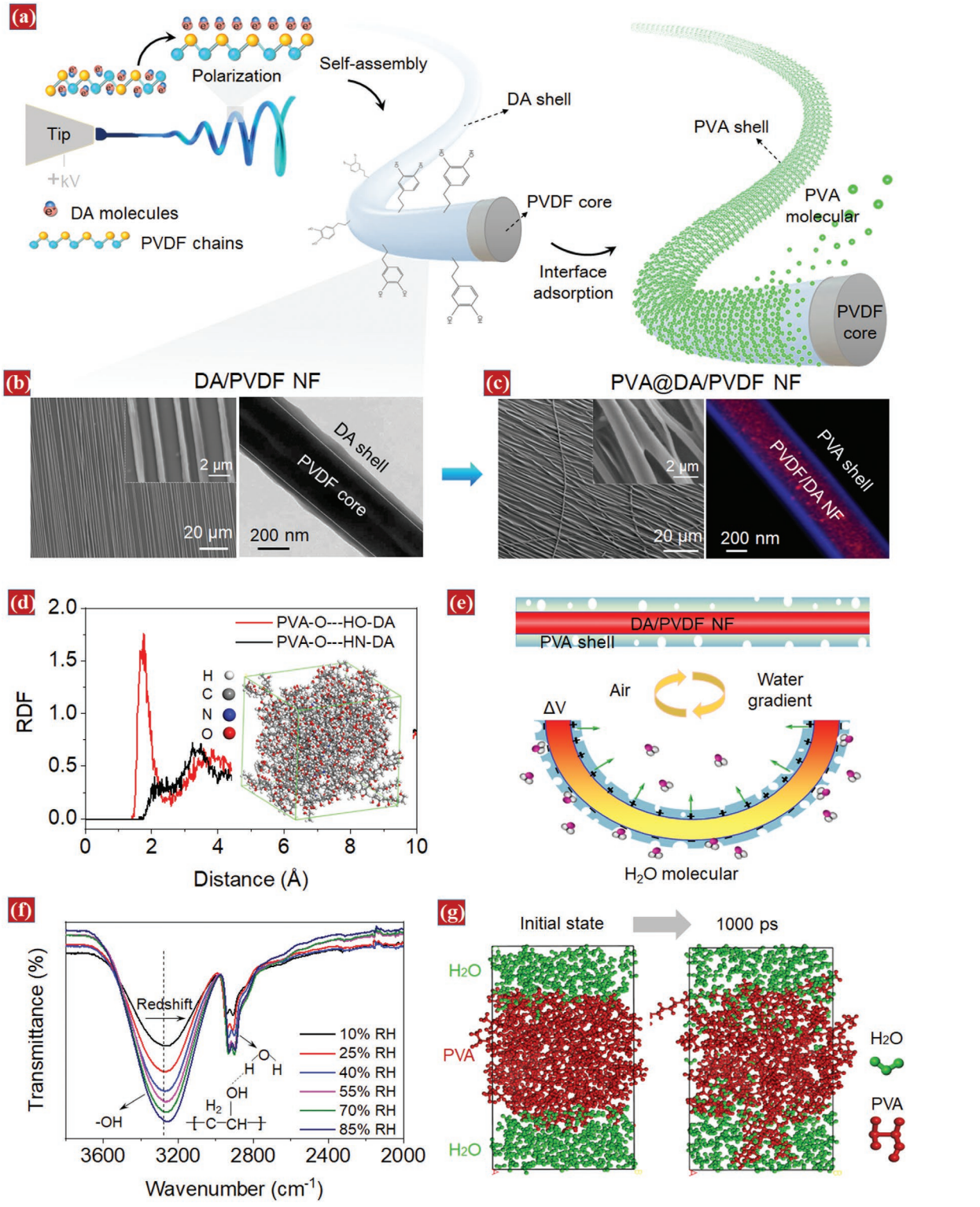

Figure 1. Fabrication process of PVA@DA/PVDF NF. a) Assembly of PVA shell onto the surface of the aligned DA/PVDF NFs by interface adsorption. b) SEM image showing DA/PVDF NFs were parallel and independent of each other. TEM image of single DA/PVDF showed shell/core structure. c) SEM image showing highly aligned PVA@DA/PVDF NFs array. LSCM image showed that PVA wrapped DA/PVDF NF. Blue: CdSe/ZnS, red: Rhodamine B. d) RDFs between the -OH groups in PVA and the -NH_2 (black) and -OH (red) groups in DA, respectively. The inset is the MD simulations of a PVA/DA molecular structure in equilibrium, showing the shell (PVA)-core (DA) arrangement. e) The uneven diffusion of water molecules in the PVA leading to the actuation behavior. f) FTIR spectrums of PVA films under varying humidity from 10 to 85%. g) MD simulations showing that the diffusion of water molecules in PVA.

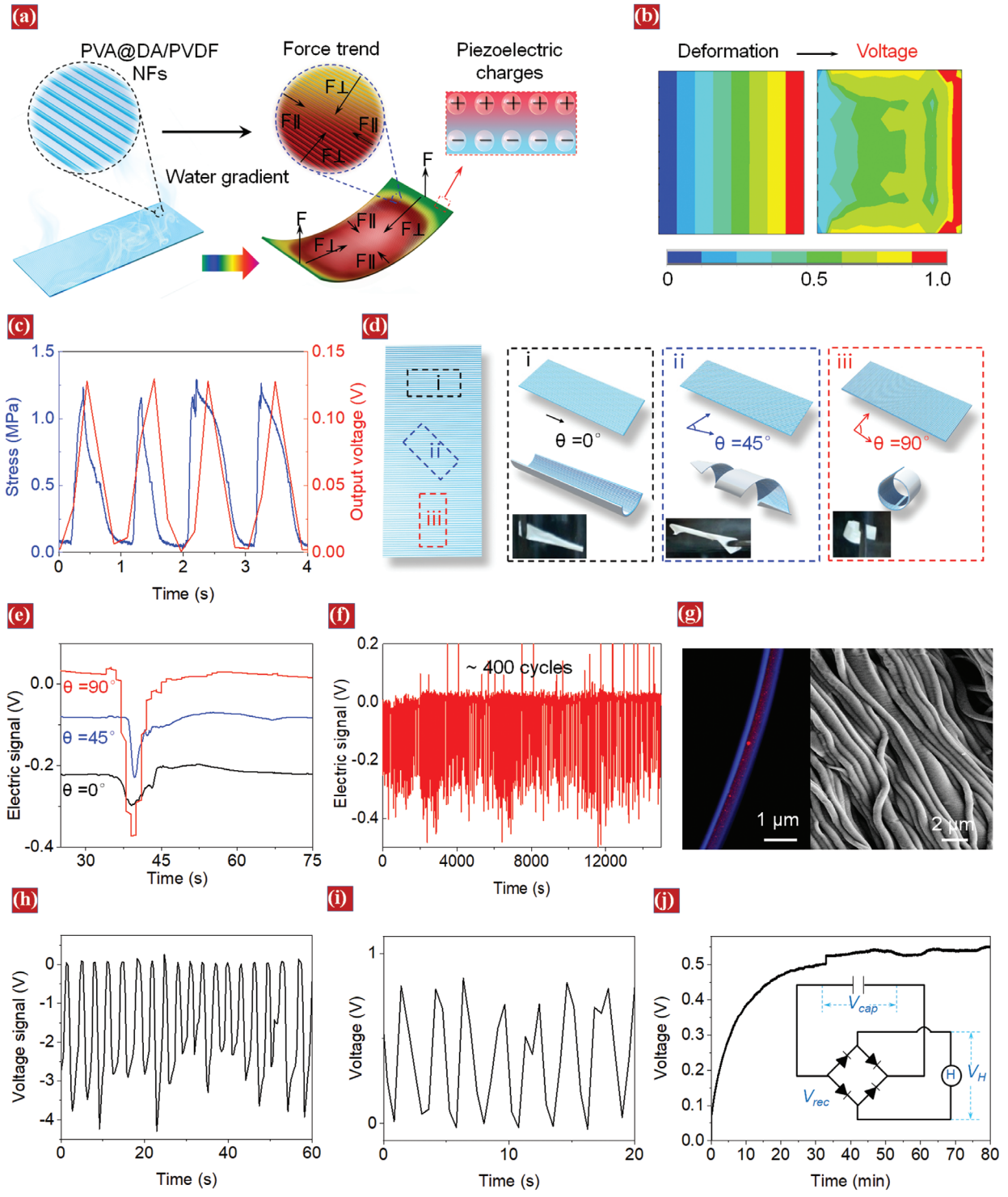

Figure 2. Programmable PVA@DA/PVDF NFs. a) Schematic illustration of the mechanism of apheliotropic bending. Contraction stress predominates in the longitudinal direction. b) The normalized deformation and voltage contours of PVA and PVDF composite film under uniform stress. c) The PVA@PVDF/DA NFs extracting mechanical forces from cyclic humidity changes of ≈1% and converting them into electric power. d) The highly aligned PVA@DA/PVDF NFs were cut into strips with 0°, 45°, and 90° concerning the long axis direction of the film. e) Output voltage profiles of PVA@DA/PVDF NFs induced by the dynamic humidity fluctuations, which showed the process of moisture absorption and desorption. f) The voltage profiles showing that the reversible motion of the PVA@DA/PVDF film with 90° proceeds continually for more than 400 times without apparent fatigue. g) The DA/PVDF NFs wrapped by PVA were still aligned arrays after repeated bending and relaxation deformation. h) Voltage outputs driven by fast-moving speed water surface. i) Voltage outputs after load 10-megohm resistor. j) Voltage across a capacitor when being charged by the HAPG. The inset was a circuit diagram for sustained powering.

(Figure S7, Supporting Information). The movable side of the tensile tester was 20 mm away from the base to keep it in contact with the film. Throughout the measurement process, the gauge length was maintained constant to collect the actuation force yielded when the film absorbed moisture. As a result, when a water-soaked filter paper approached the film, the film extracted a stress of ≈1.2 MPa from this slight water gradient difference of ≈3% and synchronously converts them into an output voltage of ≈0.13 V (Figure 2c). These data confirmed that PVA@DA/PVDF NFs could effectively extract mechanical energy from the fluctuations in ambient humidity and simultaneously convert it into electric power.

To screen the optimal pattern, the PVA@DA/PVDF films were readily cut into strips with different NFs orientations but the same aspect ratio (Figure 2d). These directions were defined by the long axis of the strip, and the relative angle was designed as 0°, 45°, and 90°, respectively. We fixed these strips over a container with water, and the water surface moved towards the strips at a slow speed of ≈6 mm s^{-1} (Figure S8a, Supporting Information). This would result in an ambient humidity fluctuation of ≈8% near the strips (Figure S8b, Supporting Information). When the ambient moisture changed, anisotropic swelling caused the strip to bend, and its bending direction was mainly regulated by the direction of NFs (Figure 2d, Movie S1, Supporting Information). The electric power converted from bending mechanical energy was collected from all strips, in which the strip with 90° yielded the highest value of 0.4 ± 0.1 V (Figure 2e, Figure S9, Supporting Information). This indicated that the strip with 90° had the most efficient humidity fluctuation-electric conversion efficiency. This was attributed to the least bending resistance and the greatest swellability in the transverse direction (i.e., 90° to the longitudinal axis).[16] The single cycle time of the ≈20 s calculated from the voltage curve closely matched well to the recording time of the video (Movie S1, Supporting Information). Besides, the PVA@DA/PVDF NFs could detect the microscopic or even invisible sudden and gradual actuation behaviors induced by the fluctuations in ambient humidity, as clearly reflected in the collected voltage profiles with some unsmooth turning points. The reversible motion proceeded continually for >400 cycles under the same operating conditions as above (Figure 2f). The output signal remained at the constant ≈0.4 V without obvious observable changes, and the PVA@DA/PVDF NFs showed no obvious damage including their high orientation and core-shell structure (Figure 2g, Figure S10, Supporting Information). It should be noted that the strip can also respond to the rapid ambient moisture change (average speed 80 mm s^{-1}, Movie S2, Supporting Information) and yielded a greater output voltage of ≈3 V (Figure 2h). Moreover, the generated alternating electric pulses were rectified using a commercial full-wave bridge rectifier, then stored in a 10 μF capacitor. A 10-megohm resistor was loaded onto this system, and the peak output reached ≈1.0 V (Figure 2i). Within 35 min of charging, the voltage of the capacitor was saturated to ≈0.55 V (Figure 2j). This was lower than the peak output voltage, possibly due to voltage drop across the rectifying diodes and/or current leakage of the capacitor. This system could use ubiquitous low-temperature water gradients as its energy source, in contrast to state-of-the-art piezoelectric energy scavengers that rely solely on mechanical vibration energy. Thus, this electromechanical coupling and humidity-actuated two-in-one PVA@DA/PVDF NFs demonstrated potential applications as sensors, switches, and power sources for low-power devices. These features encouraged the selection of the strip with 90° as the core component of HAPG.

Next, PVA@DA/PVDF NFs were tested in a natural environment to respond to the subtle fluctuations in ambient humidity caused by one water droplet. The ambient moisture fluctuations of ≈5% near the PVA@DA/PVDF NFs drove it to travel unilaterally toward the side with higher humidity at an average speed of 10 mm min^{-1} (**Figure 3**a, Figure S11, Movie S3, Supporting Information). This moisture fluctuation yielded an electric output of up to ≈0.5 V (Figure 3b). These one-way walking dynamic behaviors from overcoming resistance to moving were precisely and real-time recorded by the collected voltage profiles. Our PVA@DA/PVDF NFs was not restricted by the environment of liquid water source, it could convert ambient humidity fluctuations caused by a gentle breath out (≈47%, ΔRH), stertor (≈34%, ΔRH), and speaking (≈40%, ΔRH) behaviors into electric power (Figure 3c,d). The collected voltage profiles could identify the characteristic patterns of different breathing behaviors, as well as recorded the irregular stress rebound behavior (the right of Figure 3d, Movie S4, Supporting Information). It should be noted that all these slight water gradient differences yielded a high output voltage of >0.4 V. These data indicated that the PVA@DA/PVDF NFs possessed high sensibility and stability, as well as outstanding humidity fluctuation selectivity.

To further confirm the sensitivity and accuracy of PVA@DA/PVDF NFs to non-liquid water source-derived moisture fluctuations, the human palm was chosen as a confirmatory experiment. Figure 3e showed a schematic diagram of electric power generated in response to water gradient fluctuations caused by a moving palm. To begin with, when the palm was approaching the PVA@DA/PVDF NFs, the increased moisture was converted into electric power. Once the palm was moving away, the water gradient gradually balanced, resulting in the humidity-responsive layer returning to its initial state, and finally, the piezoelectric charge returned to an equilibrium state (Figure S12a, Supporting Information). Five minutes before the test, each volunteer participating in the test needs to touch the grounded copper wire to discharge the body's static electricity, thereby reducing the interference of static electricity on the device. Figure 3f showed voltage profiles generated by the PVA@DA/PVDF NFs during the process of human palm with skin moisture of 45% approaching and moving away at different vertical distances from 5 mm to 25 mm. At a vertical distance of 5 mm, the approaching of the palm toward the film yielded voltage of up to 81 mV, while the voltage output was gradually decreased to 0 mV as the palm moved away. While a workable distance of 5–20 mm was determined to achieve high humidity-responsive function, the film was still capable of yielding a voltage of 25 mV at a vertical working distance of 25 mm. These signals could be used for a direct analysis without an external signal amplifier. These piezoelectric voltage outputs decreased as the distance increased, showing a good linear relationship with a slope of −2.67 (red, Figure 3g). This was because the ambient humidity fluctuations and the distance showed a linear relationship with a slope of −0.38 (blue, Figure 3g, Figure S12b,

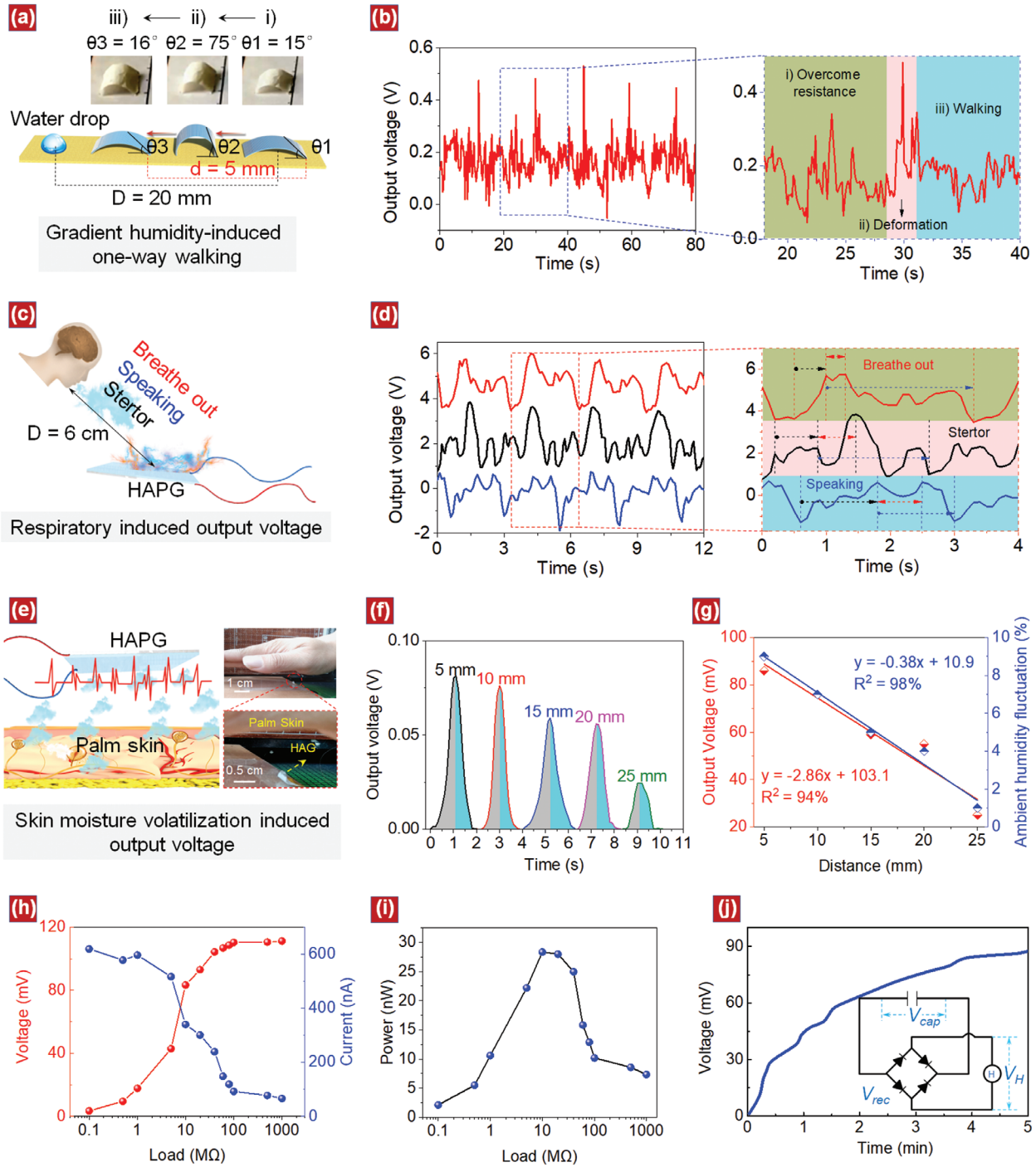

Figure 3. The response performance of the PVA@DA/PVDF NFs to ambient humidity fluctuations. a) Schematic and snapshots of one-way walking of PVA@DA/PVDF film induced by humidity fluctuations around a drop of water. b) The output voltage profiles of PVA@DA/PVDF NFs during the one-way walking, which recorded the subtle deformation process in every cycle of walking. c) Schematic of PVA@DA/PVDF NFs sensing the humidity fluctuations under the gentle respiratory behaviors. d) The output voltage profiles of PVA@DA/PVDF NFs induced by breath out, stertor, and speaking, and their wave characteristics corresponding to these respiratory behaviors. Black, red, and blue arrows indicated adsorption, stress rebound, and water desorption process of PVA@DA/PVDF NFs, respectively. e) Schematic diagram of electric power generated by PVA@DA/PVDF NFs as the palm was approaching and leaving the film in the horizontal direction. f) Voltage profiles measured decreasing with the palm moving away from the film at the different working distances between palm and film (skin moisture content: 45%, working frequency: ≈0.5 Hz). g) The distance between the palm and PVA@DA/PVDF NFs showing a linear relationship with the voltage outputs and ambient humidity fluctuations. h) The current, voltage, and i) peak power of HAPG under different outer load resistance. The palm skin moisture content is 50%, the movement frequency is 0.5 Hz, and the vertical distance is 5 mm. j) Voltage across a 1 μF capacitor when being charged by the HAPG. The inset was a circuit diagram for sustained powering. All the above working distances refer to the vertical distance between the palm and the film, the RH of the air is 43%.

Supporting Information). To further evaluate the ability of PVA@PVDF/DA NFs to sense moisture fluctuations, we also studied the effects of skin moisture content and moisture fluctuation frequency on the output voltage. The voltage outputs increased as the skin moisture and the frequency of moisture fluctuations rose (Figure S13, Supporting Information). Additionally, the palm with the antistatic rubber glove, moving on the upper side of the film at a frequency of 1 Hz and a vertical distance of 10 mm, did not induce any obvious regular voltage signals (<< 10 mV, Figure S14, Supporting Information). This confirmed that the airflow generated by the moving palm would not affect the function of the film. Next, we tried to convert the mechanical energy induced by the humidity fluctuations (skin moisture content: ≈50%) into electrical energy and store it in a 1μF capacitor (Figure 3 h–j). The vertical distance between the palm with a movement frequency of 0.5 Hz and the PVA@DA/PVDF film was 5 mm. The output current, output voltage, and peak power were investigated. Obviously, a maximum power value of ≈29 nW was achieved when the matched resistance was 10 megohm. Therefore, a 10 megohm resistor was loaded into the charging circuit. Within 5 min of charging, the voltage of the capacitor was saturated to ≈90 mV, which was expected to power some miniature wearable electronics such as microlocators, watches, etc.

To further verify the sensitivity of PVA @DA/PVDF NFs to humidity fluctuations, we chose mental sweating for yielding the non-liquid water-derived continuous moisture fluctuations that drove HAPG to generate a continuous electric power (**Figure 4**a). Unlike intermittent thermal sweating, mental sweating was usually continuous as long as emotion fluctuated.[17] This continuous mental sweating usually occurred in the palm, sole, armpit, and forehead.[18] Considering the feasibility of practical operation, the palm was chosen as a mental sweating area for yielding the non-liquid water-derived continuous moisture fluctuations. The PVA@DA/PVDF film (8 mm × 5 mm × 48 μm) assembled with breathable microporous polytetrafluoroethylene (PTFE) cap (pore size of 0.22 μm) was placed above the palm with a vertical distance of 5 mm, which could avoid the deposition of chemical components or grease from the skin onto NFs by direct contact (Figure S15, Supporting Information), maintain its dynamic balance of moisture.

First, Chinese acupuncture stimulation as an exemplary demonstration of the external stimulus was employed to yield mental sweat, and the volunteers (Feng: 38 years old, male; Zhang: 24 years old, male; and Li: 26 years old, male) experienced the stimulation in plantar position >3 times. The acupuncture stimulation triggered obvious voltage (> 0.41 V), and each stimulation yielded one set of voltage profiles (Figure 4b). From accurate timing equipment, the time point of voltage profiles matched well to the stimulus. And the interval time between the start and end of one-cycle signal was 1–3 s, matching well to the opening and closing time of palm sweat glands (Movie S5, Supporting Information), which indicates that PVA@DA/PVDF NFs timely responded to the mental sweating caused by acupuncture. Next, a sudden startled of unexpected loud sound stimulation as another example of external stimulation was used to activate sweat glands on the palm. Similarly, the HAPG yielded significant voltage pulses (Figure 4c). Differently, the voltage outputs (Feng: 0.90 ± 0.05 V vs Zhang: 1.05 ± 0.10 V vs Li:1.25 ± 0.10 V) were significantly higher than that of acupuncture stimulation (Feng: 0.61 ± 0.12 V vs Zhang: 0.41 ± 0.05 V vs Li: 0.92 ± 0.13 V). This probably because non-contact stimuli gave rise to the more sudden and intense sweat secretion (Movie S6, Supporting Information). These data showed that PVA/DA/PVDF NFs were able to sense subtle moisture fluctuations caused by mental sweat and converted them into electric power. Also, the voltage outputs generated by these external stimuli were far greater than the 0.2 V required for self-charging to re-establish the voltage.

Different from mental sweating induced by external stimuli, internal physiological activities that existed in our normal daily life were usually accompanied by weaker mental sweating. In order to verify its universality in real-world applications especially for wearable electronics, PVA@DA/PVDF film was further evaluated by sensing weaker mental sweating. Deep-breathing, a typical internal physiological activity, was used to activate sweat glands (Movie S7, Supporting Information). Although the self-controllability and predictability of deep breathing weakened the activity of sweat glands, the PVA@DA/PVDF NFs still precisely sensed the slight moisture fluctuations. The PVA@DA/PVDF NFs yielded voltage outputs of >0.2 V with the same frequency as deep breathing (Figure 4d). The respiratory cycle of each human subject strictly corresponded to one cycle of output voltage signals. Meanwhile, mathematical mental arithmetic was also performed to verify the capability of the PVA@DA/PVDF NFs sensing continuous mental sweat. Each mathematical calculation (Qu. 1–3) was raised in turn from time to time until the answer from these three human subjects (Figure 4e). At the beginning of the mathematical calculation being raised, a strong voltage peak of ≈0.1 V was activated, then followed by gradually decreasing jump waves. After the answer was given, the output voltage tended to be stable. These voltage profiles recorded and reflected the whole process of sweat secretion (Movie S8, Supporting Information). Similar voltage profiles yielded continuously when every one of the subjects engaged in this complex psychological activity. These data demonstrated that our electromechanical coupling and humidity-actuated two-in-one PVA@DA/PVDF NFs possessed high sensitivity and selectivity to moisture fluctuations induced by mental sweat, and could convert these non-liquid water source-derived continuous moisture fluctuations into electric power.

The high sensitivity to humidity fluctuations of the PVA@DA/PVDF NFs allowed the recording of detailed typical sweat damping oscillation curve features, which were known to have resulted from the subtle activity of the vagal excitation in the central nervous system (CNS, **Figure 5**a). Here, the voltage profiles of acupuncture stimulation and deep breathing were respectively chosen as the typical representatives of passive and active vagal excitation. The piezoelectric voltage signals obtained from acupuncture stimulation exhibited a profile comparable to the typical sweat damping oscillation curves (Figure 5b). Not affected by individual differences, they all displayed typical damping oscillation curves with 5 characteristic peaks. However, due to the individualized difference in sweat gland secretion, all sweat damping oscillation curves exhibited different damping oscillation waveforms of vagus excitation in peak intensity, width, and shape.

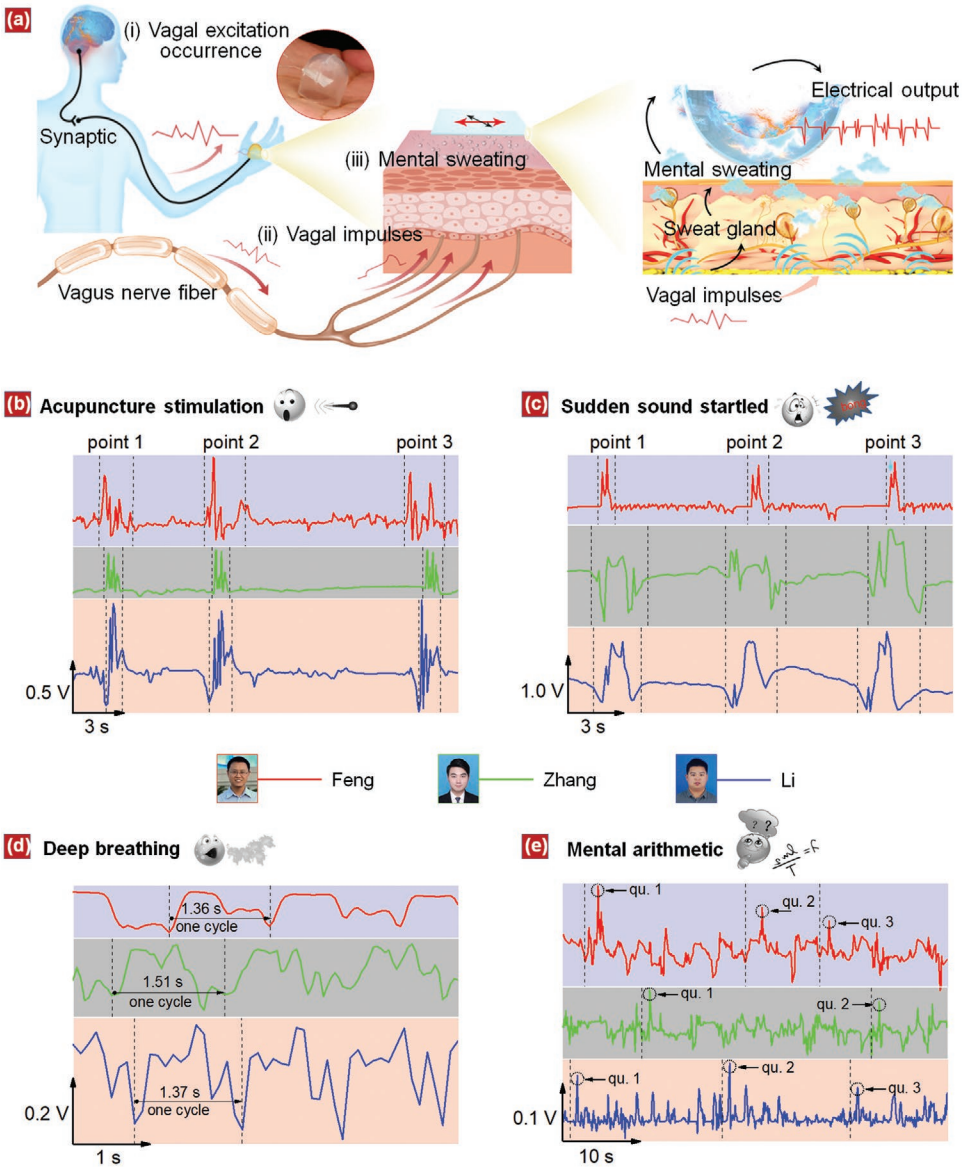

Figure 4. Continuous power generation from fluctuations in ambient humidity from mental sweat. a) Schematic diagram of the mental sweat secreted from the human palm driving the HAPG to yield electric power. Physiological pathway for vagal excitation induced mental sweating: i) Vagal excitation occurrences in the central nervous system (CNS) under physical or psychological stress; ii) then, transmits from the cerebral cortex to the mental sweat area via vagus nerve fiber; iii) and results in instantaneous sweat secretion from sweat glands in the palm (i.e., mental sweating). Power generation from four typical fluctuations in mental sweat simulated by b) acupuncture stimulation, c) sudden sound startled, d) deep breathing, and e) mental arithmetic.

These differences were counted as shown in Figure 5d. The significant differences in occurrence time (interval time 1–4, 0.89 s for Feng vs 0.75 s for Li vs 0.79 s for Zhang) and especially recovery time (interval time 4–5, 0.66 s for Feng vs 0.25 s for Li vs 0.13 s for Zhang) of vagal excitation. In addition, the piezoelectric voltage signals obtained from deep breathing also presented typical sweat damping oscillation curves (Figure 5c). However, compared with acupuncture stimulation, due to lack of an external signal responding process in the neural reflex arc (Figure 5d), the waveform of the deep breathing presented only 4 characteristic peaks (occurrence: peaks 1'–3', recovery: peaks 3'–4'). The difference was that Feng displayed the fastest occurrence and recovery time (interval time 1'–4', Total time') of vagal excitation comparing to that of acupuncture stimulation (Figure 5e), which meant that Feng had a more sensitive nerve reflex arc for the occurrence, transmission, and recovery of active vagal excitation. Obviously, these analyses proved that the collected voltage profiles were highly consistent with the characteristics of the sweat damping oscillation curves. Also, from these voltage profiles, we observed personalized information about sweat secretion. To further extract subtle personalized differences, Discrete Fourier Transformation (DFT) filter was performed to obtain frequency features (quantitative differentiation) from these voltage profiles (Figure S16,

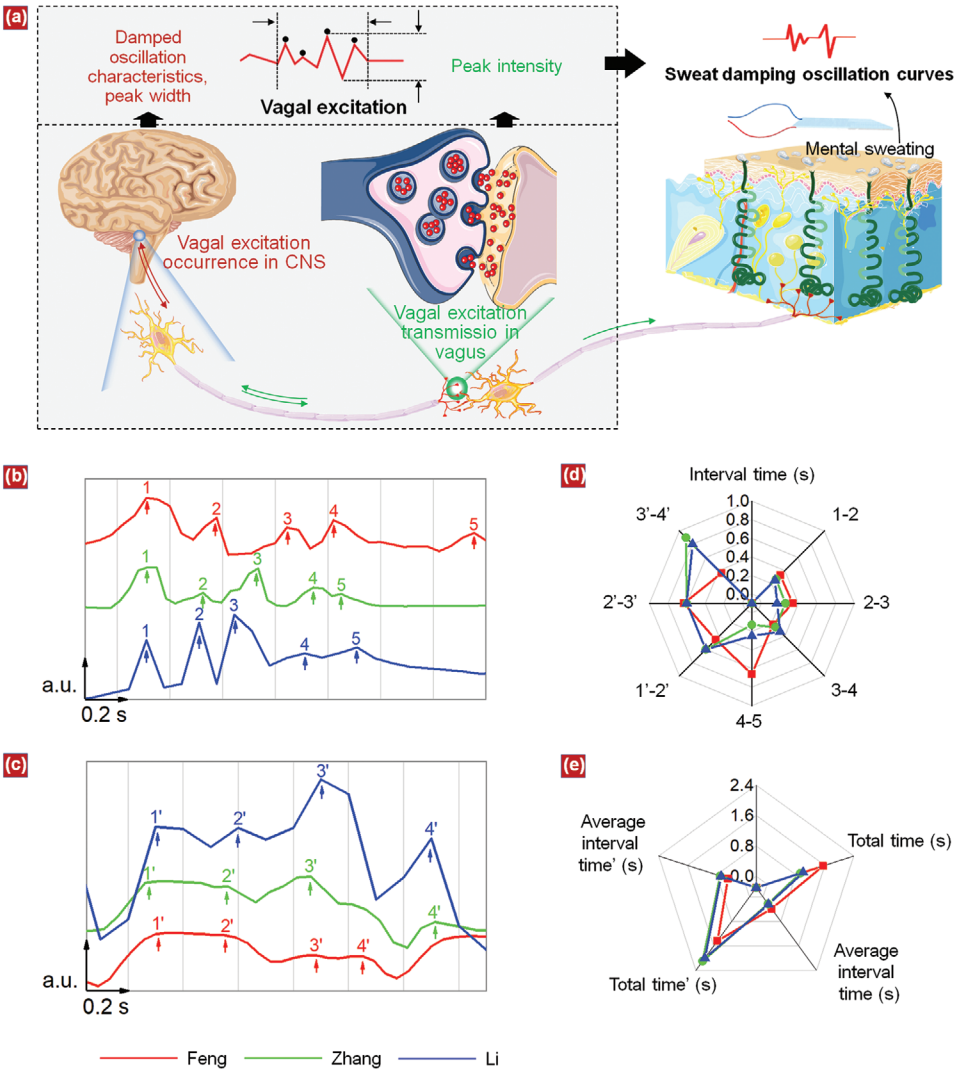

Figure 5. Personalized typical sweat damping oscillation curves extracted from collected voltage profiles. a) Schematic of neural reflex arc induced personalized sweat secretion. Damping oscillation waveform and characteristic peaks of mental sweat caused by b) body emergency response and c) physiological self-regulation. d) Interval time between characteristic peaks. e) Total time of occurrence and transmission of a vagal excitation, and the average interval time between characteristic peaks.

Supporting Information). It could be found that DFT-transformed curves exhibited stronger regularity and specificity as compared to original voltage profiles (Figures S17 and S18, Supporting Information), which were easily recognized by various external microelectronic processors. This abundant personalized information could be precisely distinguished and recognized from the collected voltage profiles, thus again confirming the sensitivity, selectivity, and accuracy of PVA@DA/PVDF NFs to subtle moisture fluctuations.

3. Conclusion

In summary, we developed an electromechanical coupling and humidity-actuated two-in-one HAPG composed of PVA-wrapped highly aligned DA/PVDF shell/core NFs. The highly aligned DA/PVDF NFs were fabricated by one-step electrospinning on large scale, which had been proven to have high piezoelectric properties. Therefore, high sensitivity to weak actuation deformation was guaranteed. Because of the strong interfacial adsorption between PVA and hydrophilic groups on DA, the PVA shell can be introduced around the interface of DA/PVDF NFs by simple suction filtration. Such electromechanical coupling and humidity-actuated two-in-one HAPG showed excellent stability and avoided the potential delamination risk compared with other bilayer actuators. As-received PVA@DA/PVDF NFs exhibited superb sensitivity and selectivity to humidity fluctuations with excellent stability. It could exchange moisture with the ambient humidity (e.g., moving water surface, one drop water, and human respiratory behaviors) to perform expansion and contraction and automatically convert them into electric power. An all-fiber-based

portable HAPG was fabricated and tested on human palm skin. As a result, the devices showed high sensitivity and accuracy for detecting subtle fluctuations in the ambient humidity induced by various mental sweating and converted these non-liquid water source-derived continuous moisture fluctuations into electric power. The electrical energy could be stored in capacitors, which were expected to power wearable micro- and nano-electronic devices.

4. Experimental Section

Fabrication of Highly Aligned DA/PVDF NFs: The electrospun solution of DA/PVDF NFs was formulated according to the recent report. Briefly, the electrospinning solution was prepared by dissolving 0.2 g mL^{-1} PVDF powder (MW = 5.34 kDa, Macklin Biochemical Co., Ltd.) in a mixture solution of DA (98%, Mai Ruier Chemical Technology Co., Ltd.) and DMF (DA/DMF, 2mg mL^{-1}) under sonication for 90 min. The electrospinning was conducted using a high DC voltage of 1.2 kV cm^{-1} with a solution flow speed at 1 mL h^{-1} at room temperature and 35% humidity. As-received NFs were stored in vacuum for further experimental operation. The standard laboratory setup consists of a spinneret connected to a high-voltage power supply, a syringe pump, and an aluminum U-shaped tube.

Fabrication of PVA@DA/PVDF NFs: PVA (MW = 44.1 kDa, Aladdin Bio-Chem Technology Co., LtD) was dissolved in deionized water at 90 °C for 24 h at a polymer/solvent concentration of 2% w/v. A vacuum filtration device was used to repeatedly filter the PVA solution three times, and finally, a PVA shell of about 50 nm was successfully introduced on the DA/PVDF NFs.

MD Simulation of PVA and DA: The periodic MD simulation was carried out using the Material Studio software program to explore the RDF of pristine PVA/DA composites. A total of 58 PVA chains and 28 DA molecules were adopted to construct the simulation system, with each PVA chain comprised of 20 monomers. The COMPASS (condensed-phase optimized molecular potentials for atomistic simulation studies) force field was used and all simulations were conducted with a time step of 1 fs. All models were allowed to evolve dynamically in the constant pressure/temperature (NPT) ensembled at 298 K and 1 GPa or 1atm pressure. In all simulations, the temperature and pressure of the system were maintained by the Andersen stochastic collision and barostat with periodic boundary conditions and fixed linear momentum, and the vdW interactions were truncated at 10 Å with long-range tail corrections. The converged density of the PVA/DA cell was obtained by using the high-low pressure dynamics simulation method, and the total simulation time of high or low pressure was 1 ns respectively, then the NPT simulation was conducted for 1ns at 298 K and 1atm to collect data. Since DA contained a large number of hydrogen donors (e.g., nitrogen and oxygen), DA enabled to massive hydrogen bonding networks with PVA.

Characterizations: The formation of hydrogen bonds between PVA and water vapor molecules in the ambient humidity from 10 to 85% were characterized by IR (Nicolet IS-10, Thermo Fisher Scientific). The morphology and structural distribution were observed by SEM (Supra 55, Carl Zeiss) and TEM (JEM-2100, JEOL). The stress-strain curves were performed with a tensile tester (HY-0580). In order to observe the distribution of PVA and DA/PVDF NFs, CdSe/ZnS (blue, Xingshuo Nano Technology Co. Ltd) and Rhodamine B (red, Sinopharm Chemical Reagent Co., Ltd) were mixed into PVA solution and DA/PVDF electrospinning solution respectively, and then PVA@DA/PVDF NFs were prepared according to the above method. The structure of the PVA@DA/PVDF NFs was determined by a laser scanning confocal microscope (LSCM, Leica SP8 Germany). In order to facilitate the finite element simulation modeling, the PVA unit and the PVDF unit were modeled and assembled using the structural element solid185 and the piezoelectric element solid226 respectively. A uniform stress was applied to the composite film of PVA and PVDF to simulate the actuation behavior. In addition, all RH data were tested by a humidity monitor based on the interdigital electrode type (Thermopro TP49).

In Situ Actuation Force Test from ≈3% Moisture Fluctuation: For testing the ability of PVA@DA/PVDF NFs with 90° (30 mm × 5 mm × 48 µm) to extract chemical potential energy from water gradients, one end of the film was fixed on the base of the tensile tester (HY-0580), and the other end was flexible and movable. The movable side of the tensile tester was 20 mm away from the base to keep it in contact with the film, and the gauge length was maintained constant throughout the measurement so that the supporting force generated only by the deformation of the film. When the water-soaked filter paper (≈3%, ΔRH) approached the PVDF/PVA bilayer, the stress increased to ≈1.2 MPa.

Electric Characterizations of the PVA@DA/PVDF NFs: The capless hollow PTFE with a pore size of 0.22 µm (50 µm) was used as the shell package to ensure the mechanical firmness and to maintain its dynamic balance of moisture. The electric profiles were measured by an electrochemical workstation (CHI 760e).

Supporting Information

Supporting Information is available from the Wiley Online Library or from the author.

Acknowledgements

T.L., F.J., and M.Q. contributed equally to this work. The authors acknowledge financial support from the National Natural Science Foundation of China (51773093 and 11204033), Postgraduate Research & Practice Innovation Program of Jiangsu Province (SJCX17_0118), and the Fundamental Research Funds for the Central Universities (No. 30920041105). T.L. thanks financial supports from China Scholarship Council (CSC: 201906840093).

Conflict of Interest

The authors declare no conflict of interest.

Data Availability Statement

Research data are not shared.

Keywords

electrospinning, energy harvesting, humidity actuators, moisture fluctuations, piezoelectric generators

Received: April 30, 2021
Revised: May 25, 2021
Published online:

[1] a) D. Gielen, F. Boshell, D. Saygin, *Nat. Mater.* **2016**, *15*, 117; b) F.-R. Fan, Z.-Q. Tian, Z. L. Wang, *Nano Energy* **2012**, *1*, 328.
[2] a) Z. L. Wang, *Nature* **2017**, *542*, 159; b) A. Cho, *Science* **2015**, *347*, 1084; c) Y. Xi, J. Wang, Y. Zi, X. Li, C. Han, X. Cao, C. Hu, Z. Wang, *Nano Energy* **2017**, *38*, 101.
[3] P. Cheng, H. Guo, Z. Wen, C. Zhang, X. Yin, X. Li, D. Liu, W. Song, X. Sun, J. Wang, Z. L. Wang, *Nano Energy* **2019**, *57*, 432.

[4] a) K. Yang, T. Pan, I. Pinnau, Z. Shi, Y. Han, *Nano Energy* **2020**, *78*, 105326; b) Y. Zhang, T. Xiong, L. Suresh, H. Qu, X. Zhang, Q. Zhang, J. Yang, S. C. Tan, *ACS Energy Lett.* **2020**, *5*, 3397; c) Y. Zhang, H. Zhang, T. Xiong, H. Qu, J. J. Koh, D. K. Nandakumar, J. Wang, S. C. Tan, *Energy Environ. Sci.* **2020**, *13*, 4891; d) X. Zhang, J. Yang, R. Borayek, H. Qu, D. K. Nandakumar, Q. Zhang, J. Ding, S. C. Tan, *Nano Energy* **2020**, *75*, 104873; e) P. Chen, J. An, S. Shu, R. Cheng, J. Nie, T. Jiang, Z. L. Wang, *Adv. Energy Mater.* **2021**, *11*, 2003066; f) Y. Feng, X. Liang, J. An, T. Jiang, Z. L. Wang, *Nano Energy* **2021**, *81*, 105625; g) H. Wang, L. Xu, Y. Bai, Z. L. Wang, *Nat. Commun.* **2020**, *11*, 4203.

[5] M. Ma, L. Guo, D. G. Anderson, R. Langer, *Science* **2013**, *339*, 186.

[6] H. Arazoe, D. Miyajima, K. Akaike, F. Araoka, E. Sato, T. Hikima, M. Kawamoto, T. Aida, *Nat. Mater.* **2016**, *15*, 1084.

[7] J. Deng, J. Li, P. Chen, X. Fang, X. Sun, Y. Jiang, W. Weng, B. Wang, H. Peng, *J. Am. Chem. Soc.* **2016**, *138*, 225.

[8] a) L. Gu, J. Liu, N. Cui, Q. Xu, T. Du, L. Zhang, Z. Wang, C. Long, Y. Qin, *Nat. Commun.* **2020**, *11*, 1030; b) L. Gu, N. Cui, L. Cheng, Q. Xu, S. Bai, M. Yuan, W. Wu, J. Liu, Y. Zhao, F. Ma, Y. Qin, Z. L. Wang, *Nano Lett.* **2013**, *13*, 91; c) T. Li, Z. Q. Feng, M. Qu, K. Yan, T. Yuan, B. Gao, T. Wang, W. Dong, J. Zheng, *ACS Nano* **2019**, *13*, 10062; d) J. Li, Y. Long, F. Yang, H. Wei, Z. Zhang, Y. Wang, J. Wang, C. Li, C. Carlos, Y. Dong, Y. Wu, W. Cai, X. Wang, *Adv. Funct. Mater.* **2020**, *30*, 2002868; e) J. Li, L. Kang, Y. Yu, Y. Long, J. J. Jeffery, W. Cai, X. Wang, *Nano Energy* **2018**, *51*, 728. f) X. Qu, X. Ma, B. Shi, H. Li, L. Zheng, C. Wang, Z. Liu, Y. Fan, X. Chen, Z. Li, Z. L. Wang, *Adv. Funct. Mater.* **2020**, *31*, 2006612; g) F. A. Hassani, Q. Shi, F. Wen, T. He, A. Haroun, Y. Yang, Y. Feng, C. Lee, *Smart Mater. Med.* **2020**, *1*, 92; h) L. Liu, Q. Shi, Z. Sun, C. Lee, *Nano Energy* **2021**, *86*, 106154.

[9] T. Li, M. Qu, C. Carlos, L. Gu, F. Jin, T. Yuan, X. Wu, J. Xiao, T. Wang, W. Dong, X. Wang, Z. Q. Feng, *Adv. Mater.* **2020**, *33*, 2006093.

[10] L. Zhang, S. Chizhik, Y. Wen, P. Naumov, *Adv. Funct. Mater.* **2016**, *26*, 1040.

[11] a) E. Reyssat, L. Mahadevan, *J. R. Soc., Interface* **2009**, *6*, 951; b) P. Egan, R. Sinko, P. R. LeDuc, S. Keten, *Nat. Commun.* **2015**, *6*, 7418.

[12] a) L. Persano, C. Dagdeviren, Y. Su, Y. Zhang, S. Girardo, D. Pisignano, Y. Huang, J. A. Rogers, *Nat. Commun.* **2013**, *4*, 1633; b) E. J. Curry, T. T. Le, R. Das, K. Ke, E. M. Santorella, D. Paul, M. T. Chorsi, K. T. M. Tran, J. Baroody, E. R. Borges, B. Ko, A. Golabchi, X. Xin, D. Rowe, L. Yue, J. Feng, M. D. Morales-Acosta, Q. Wu, I. P. Chen, X. T. Cui, J. Pachter, T. D. Nguyen, *Proc. Natl. Acad. Sci. U. S. A.* **2020**, *117*, 214.

[13] a) N. Wang, Y. Feng, Y. Zheng, L. Zhang, M. Feng, X. Li, F. Zhou, D. Wang, *Adv. Funct. Mater.* **2021**, *31*, 2009172; b) P. P. Kannan, N. K. Karthick, A. Mahendraprabu, R. Shanmugam, A. Elangovan, G. Arivazhagan, *J. Mol. Struct.* **2017**, *1139*, 196.

[14] L. Zhang, P. Naumov, X. Du, Z. Hu, J. Wang, *Adv. Mater.* **2017**, *29*, 1702231.

[15] L. T. de Haan, J. M. Verjans, D. J. Broer, C. W. Bastiaansen, A. P. Schenning, *J. Am. Chem. Soc.* **2014**, *136*, 10585.

[16] H. Lin, J. Gong, M. Eder, R. Schuetz, H. Peng, J. W. C. Dunlop, J. Yuan, *Adv. Mater. Interfaces* **2017**, *4*, 1600768.

[17] G. Havenith, D. Fiala, *Compr. Surv.* **2015**, *6*, 255.

[18] T. Kamei, T. Tsuda, S. Kitagawa, K. Naitoh, N. Koji, T. Ohhashi, *Anal. Chim. Acta* **1998**, *365*, 319.